

Cite this: *Chem. Sci.*, 2024, **15**, 3545 All publication charges for this article have been paid for by the Royal Society of Chemistry

Received 14th November 2023

Accepted 16th January 2024

DOI: 10.1039/d3sc06096a

[rsc.li/chemical-science](http://rsc.li/chemical-science)

## A polydopamine coating enabling the stable cycling of $\text{MnO}_2$ cathode materials in aqueous zinc batteries†

Guoli Zhang,<sup>a</sup> Jiaqi Zhu,<sup>a</sup> Lu Lin,<sup>a</sup> Yaozhi Liu,<sup>a</sup> Shuo Li,<sup>a</sup> Qianrui Li,<sup>a</sup> Xiao-Xia Liu  <sup>a,b,c</sup> and Xiaoqi Sun 

$\text{MnO}_2$  is a desired cathode candidate for aqueous zinc batteries. However, their cycling stability is seriously limited by active material dissolution, and pre-addition of  $\text{Mn}^{2+}$  salts in electrolytes is widely required to shift the dissolution equilibrium. Herein, we synthesize a polydopamine (PDA) coated  $\text{MnO}_2$  composite material ( $\text{MnO}_2/\text{PDA}$ ) to realize stable cycling in zinc cells without relying on pre-added  $\text{Mn}^{2+}$ . The functional groups on PDA exhibit strong coordination ability with the Mn active material. It not only confines dissolved species within the cathode during discharge, but also enhances their deposition back to the cathode during charge to retrieve the active material. Thanks to this effect, the cathode achieves 81.1% capacity retention after 2000 cycles at  $1 \text{ A g}^{-1}$  in the 1 M  $\text{ZnSO}_4$  electrolyte, superior to 37.3% with the regular  $\text{MnO}_2$  cathode. This work presents an effective strategy to realize the stable cycling of manganese oxide cathode materials in aqueous zinc batteries.

## Introduction

Rechargeable aqueous zinc batteries have attracted great attention for their low cost, high safety and environmental friendliness.<sup>1–10</sup> Zn metal is applied as the anode, providing a high capacity of  $820 \text{ mA h g}^{-1}/5855 \text{ mA h cm}^{-3}$  and low redox potential.<sup>11–13</sup> So far, the main cathode families studied for Zn batteries include Mn-based oxides, V-based oxides, polyanion materials and organic compounds.<sup>14–16</sup> Among them, manganese oxides show great promise due to their high capacity, relatively high voltage and simple preparation.<sup>17</sup> Various crystal structure control, morphology engineering and composite design methods have been applied to enhance the capacity and rate capability. Meanwhile,  $\text{MnO}_2$  has been revealed to undergo complicated energy storage processes in aqueous zinc cells, including the de/intercalation of  $\text{Zn}^{2+}$  and/or  $\text{H}^+$ , conversion reactions, and dissolution–deposition reactions.<sup>18,19</sup>

One of the most important limiting factors of manganese oxide cathode materials in zinc batteries is rapid capacity fading, which is caused by active material dissolution.<sup>20,21</sup> The main and most effective strategy for inhibiting dissolution and

promoting cycling stability is to shift the dissolution equilibrium by adding extra  $\text{Mn}^{2+}$  in electrolytes.<sup>22–25</sup> Besides, it is proposed that the introduction of pillars, *e.g.*, polyaniline and water, in layered  $\text{MnO}_2$  enhances its structural stability and improves capacity retention.<sup>26</sup> In addition, heteroatom doping and compositing with conductive compounds<sup>27,28</sup> have been reported to improve the electrochemical stability of  $\text{MnO}_2$ . Nevertheless, the majority of  $\text{MnO}_2$  studies still rely on pre-added  $\text{Mn}^{2+}$  salts in electrolytes to achieve reasonable cycling performance.

A possible concern for  $\text{Mn}^{2+}$  additives, on the other hand, is that they would be oxidized and deposited at the cathode during the charge process,<sup>29,30</sup> functioning as extra active materials. Therefore, the tests of  $\text{MnO}_2$  in electrolytes free of pre-added  $\text{Mn}^{2+}$  would reflect the cycling performance of the cathodes themselves. In addition to suppressing dissolution, an effective strategy to realize stable cycling would be the recycling of dissolved active material. This can be realized by promoting the deposition of dissolved  $\text{Mn}^{2+}$  back to the cathode and oxidation to  $\text{MnO}_2$  during the charge process. In order to achieve this goal, we herein construct a polydopamine (PDA) coated  $\text{MnO}_2$  composite material ( $\text{MnO}_2/\text{PDA}$ ). Specifically, PDA contains various active sites to coordinate with the Mn active material. It not only interacts with and confines dissolved active material at the cathode during discharge, but also facilitates the back-deposition of dissolved  $\text{Mn}^{2+}$  during charge. A stable long-term cycling of the  $\text{MnO}_2/\text{PDA}$  composite material is thus realized. It retains  $147 \text{ mA h g}^{-1}$  capacity after 2000 cycles at  $1 \text{ A g}^{-1}$  in the  $\text{ZnSO}_4$  electrolyte free of  $\text{Mn}^{2+}$  additives, corresponding to 81.1% capacity retention, superior to only  $90 \text{ mA h g}^{-1}$  capacity left (37.3% retention) for the bare  $\text{MnO}_2$  material.

<sup>a</sup>Department of Chemistry, Northeastern University, Shenyang 110819, China. E-mail: [xxliu@mail.neu.edu.cn](mailto:xxliu@mail.neu.edu.cn); [sunxiaoqi@mail.neu.edu.cn](mailto:sunxiaoqi@mail.neu.edu.cn)

<sup>b</sup>National Frontiers Science Center for Industrial Intelligence and Systems Optimization, Northeastern University, 3-11 Wenhua Road, Shenyang, 110819, China

<sup>c</sup>Key Laboratory of Data Analytics and Optimization for Smart Industry (Northeastern University), Ministry of Education, China

† Electronic supplementary information (ESI) available. See DOI: <https://doi.org/10.1039/d3sc06096a>



## Results and discussion

The standard  $\text{MnO}_2$  material was obtained by a hydrothermal reaction. To achieve a PDA coating, an *in situ* self-polymerization of dopamine was further carried out. Fig. 1a compares the X-ray diffraction (XRD) patterns of  $\text{MnO}_2$  and  $\text{MnO}_2/\text{PDA}$ . Both patterns are well fitted to the alpha-phase  $\text{MnO}_2$  (JCPDS: 44-0141),<sup>31</sup> suggesting that the coating does not affect the crystal structure of  $\text{MnO}_2$ . The morphology and microstructure of the  $\text{MnO}_2/\text{PDA}$  composite are characterized. The scanning electron microscopy (SEM) image shows a nano-rod morphology with micron-length and a diameter below 100 nm, which resembles that of the original  $\text{MnO}_2$  (Fig. 1b and S1†). Fig. 1c shows the high-resolution transmission electron microscopy (HR-TEM) image. Well-resolved lattice fringes with a spacing of 0.51 nm are present in the inner part of the nano-rod, corresponding to the (200) plane of  $\alpha$ -phase  $\text{MnO}_2$ . Meanwhile, an amorphous layer with a thickness below 2 nm is identified on the surface. The energy dispersive X-ray spectroscopy (EDS) elemental mapping reveals the uniformly

distributed Mn, C, and O on the nano-rods (Fig. 1d). This confirms that the amorphous PDA layer is homogeneously coated on the surface of  $\text{MnO}_2$ .

The composition of  $\text{MnO}_2/\text{PDA}$  is further studied. Fig. 1e shows the Fourier transform infrared spectroscopy (FT-IR) spectra of PDA and  $\text{MnO}_2/\text{PDA}$ . The characteristic vibrations of PDA are shown in the composite material, including that of C–N at 1382.4  $\text{cm}^{-1}$ , C=O at 1680.6  $\text{cm}^{-1}$ , and N–H/O–H in the range of 3000  $\text{cm}^{-1}$  to 3400  $\text{cm}^{-1}$ . Interestingly, these vibrations experience a redshift in comparison to those of bare PDA. Meanwhile, the Mn–O vibration in  $\text{MnO}_2/\text{PDA}$  shows up at 633.3  $\text{cm}^{-1}$  in the Raman spectrum, which is blueshifted compared to that at 630.8  $\text{cm}^{-1}$  in bare  $\text{MnO}_2$  (ref. 32 and 33) (Fig. 1f). These changes suggest the coordination between  $\text{MnO}_2$  and PDA at the interface and confirm their strong interactions in the composite material.<sup>34,35</sup> Fig. 1g–i and S2† show the X-ray photoelectron spectroscopy (XPS) spectra of  $\text{MnO}_2/\text{PDA}$ . The C–N peak is identified at 399.8 eV in the N 1s spectrum, and C–O and C=O components are found at 531.2 eV and 532.7 eV in the O 1s spectrum, respectively.<sup>36</sup> These species are

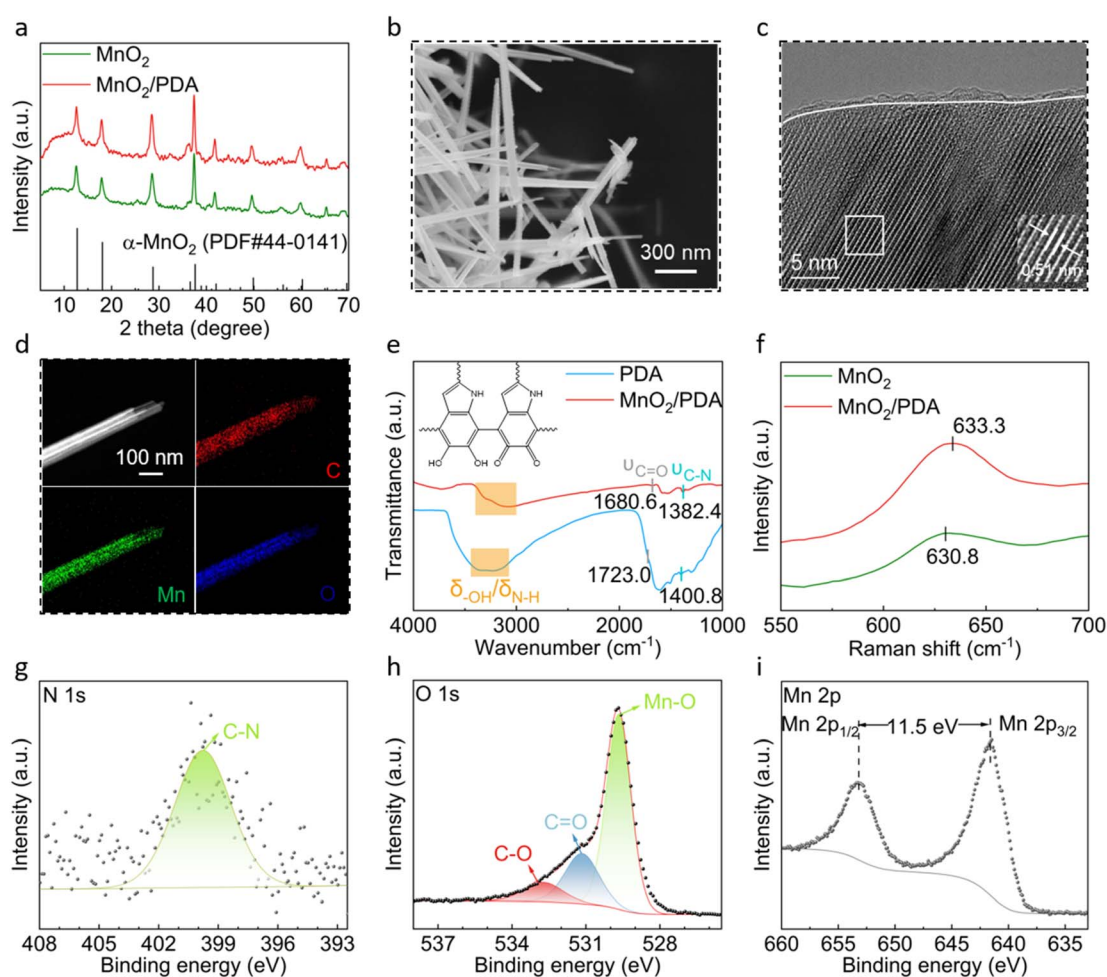


Fig. 1 (a) XRD patterns of  $\text{MnO}_2$  and  $\text{MnO}_2/\text{PDA}$ . (b) SEM image, (c) HR-TEM image and (d) EDS mapping of  $\text{MnO}_2/\text{PDA}$ . (e) FT-IR of PDA and  $\text{MnO}_2/\text{PDA}$  (inset shows the chemical structure of PDA). (f) Raman spectra of  $\text{MnO}_2$  and  $\text{MnO}_2/\text{PDA}$ . (g) N 1s, (h) O 1s, and (i) Mn 2p XPS of  $\text{MnO}_2/\text{PDA}$ .



also present in the C 1s spectrum. Besides, a third O peak is revealed at 529.7 eV in the O 1s spectrum. This corresponds to the lattice oxygen in  $\text{MnO}_2$ . In the Mn 2p spectrum, the splitting energy between the  $2p_{3/2}$  and  $2p_{1/2}$  peaks is 11.5 eV, which matches well with that of the typical  $\text{MnO}_2$  material.<sup>37–39</sup> Thermogravimetric analysis (TGA) is performed for the  $\text{MnO}_2$ /PDA composite. As shown in Fig. S3,† the decomposition of PDA takes place after 300 °C, and its weight percent is estimated to be 12%. The molecular weight of PDA is measured to be 1105 with a polydispersity of 3.8 by gel permeation chromatography (GPC).

The electrochemical performance of  $\text{MnO}_2$  and  $\text{MnO}_2$ /PDA cathode materials is studied in zinc cells. The 1 M  $\text{ZnSO}_4$  aqueous solution free of  $\text{Mn}^{2+}$  additives is applied as the electrolyte to evaluate the stability of the cathodes themselves. Galvanostatic charge and discharge is first carried out at a relatively low current density of 0.1  $\text{A g}^{-1}$ . As shown in Fig. 2a, the  $\text{MnO}_2$  cathode delivers a capacity of 323  $\text{mA h g}^{-1}$  in the first cycle, but it decays significantly in subsequent cycles. Only 222  $\text{mA h g}^{-1}$  capacity is left after 100 cycles. This poor cycling stability is typical for regular  $\text{MnO}_2$  cathode materials in aqueous zinc cells, resulting from irreversible active material dissolution. In comparison, the  $\text{MnO}_2$ /PDA cathode presents much improved stability. The capacity drops slowly from 300  $\text{mA h g}^{-1}$  to 265  $\text{mA h g}^{-1}$  over 100 cycles (Fig. 2b and S4†). The rate performance is studied for the two cathodes (Fig. 2c–e). The  $\text{MnO}_2$  cathode again experiences capacity decay at various current densities, and it is more serious at lower current densities. This is attributed to the longer time for the dissolution process at slower rates. Only 92  $\text{mA h g}^{-1}$  capacity is left upon the increase of current density to 2  $\text{A g}^{-1}$ , and a poor capacity of 224  $\text{mA h g}^{-1}$  is recovered with the decrease of current density back to 0.1  $\text{A g}^{-1}$ . The  $\text{MnO}_2$ /PDA cathode material, in contrast, presents stable capacity retentions at different current densities. The capacities of 278, 257, 220, 164

and 134  $\text{mA h g}^{-1}$  are obtained at 0.2, 0.3, 0.5, 1 and 2  $\text{A g}^{-1}$ , respectively. With the return of current density to 0.1  $\text{A g}^{-1}$ , a high capacity of 304  $\text{mA h g}^{-1}$  is still retained.

Long-term cycling is carried out at 1  $\text{A g}^{-1}$  (Fig. 2f). The  $\text{MnO}_2$ /PDA cathode again presents better cycling performance. The capacity undergoes a short degradation period followed by a gradual increase in subsequent cycles. Considering the complicated energy storage processes of the  $\text{MnO}_2$  active material, including one electron transfer and two electron transfer as well as irreversible dissolution of  $\text{Mn}^{2+}$  in the electrolyte, repeated cycles are required for the stabilization of these processes.<sup>40</sup> The capacity finally reaches 147  $\text{mA h g}^{-1}$  after 2000 cycles, which is 81.1% that of the initial cycle. This is superior to the  $\text{MnO}_2$  cathode, with fast capacity decay during early cycles (Fig. S5†) and only 90  $\text{mA h g}^{-1}$  capacity retained after 2000 cycles. The above analysis demonstrates the largely improved electrochemical performance of the  $\text{MnO}_2$  cathode material in aqueous zinc cells with the help of a PDA coating.

Electrochemical impedance spectroscopy (EIS) is carried out for the  $\text{MnO}_2$  and  $\text{MnO}_2$ /PDA electrodes to study the reaction kinetics. Fig. 3a compares the Nyquist plots at 25 °C. It reveals a charge transfer resistance ( $R_{ct}$ ) of 24 ohm for  $\text{MnO}_2$ , which largely reduces to 10 ohm for  $\text{MnO}_2$ /PDA. EIS is then performed at various temperatures. As shown in Fig. 3b and c, the semi-circles of  $\text{MnO}_2$ /PDA all exhibit smaller radii to the ones of  $\text{MnO}_2$ , suggesting the smaller charge transfer resistance of the former at different temperatures. The activation energy ( $E_a$ ) is further calculated from the linear fits of  $\ln(R_{ct}^{-1})$  versus  $1/T$  plots according to the Arrhenius equation (Fig. 3d). The activation energy of the  $\text{MnO}_2$ /PDA cathode is calculated to be 32.8  $\text{kJ mol}^{-1}$ , which is lower than 40.9  $\text{kJ mol}^{-1}$  of the  $\text{MnO}_2$  cathode. This suggests that the reaction kinetics of the  $\text{MnO}_2$  material is effectively enhanced with the help of a PDA coating. This is attributed to the facilitated desolvation process of  $\text{Zn}^{2+}$  and  $\text{H}^+$  by PDA, which coordinates with  $\text{Zn}^{2+}$  and forms

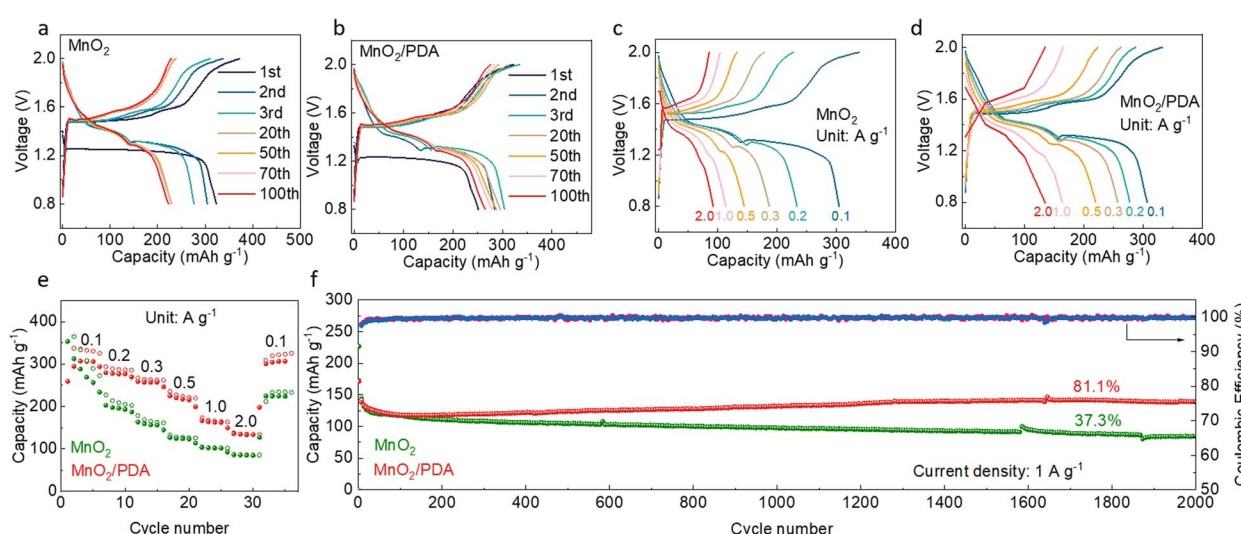


Fig. 2 Electrochemical performance of different cathodes in aqueous zinc batteries with 1 M  $\text{ZnSO}_4$  electrolyte: charge/discharge curves of (a)  $\text{MnO}_2$  and (b)  $\text{MnO}_2$ /PDA at different cycles at 0.1  $\text{A g}^{-1}$ ; charge/discharge curves at different current densities of (c)  $\text{MnO}_2$  and (d)  $\text{MnO}_2$ /PDA and (e) their capacities; (f) long-term cycling performance of  $\text{MnO}_2$  and  $\text{MnO}_2$ /PDA at 1  $\text{A g}^{-1}$ .



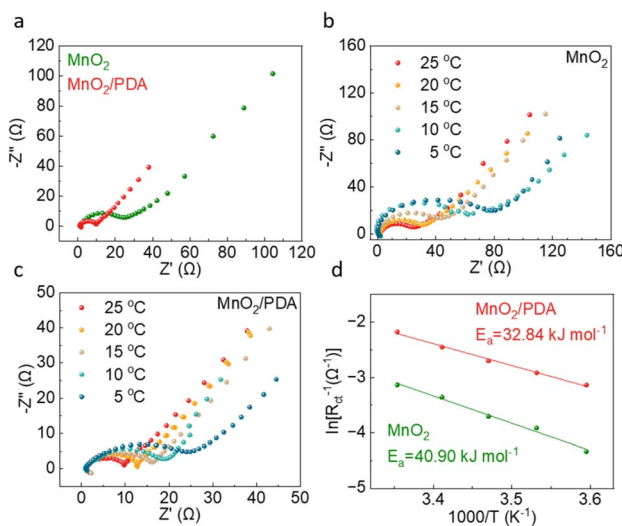


Fig. 3 EIS of  $\text{MnO}_2$  and PDA/ $\text{MnO}_2$ : (a) the comparison of Nyquist plots at 25 °C; the Nyquist plots at various temperatures of (b)  $\text{MnO}_2$  and (c)  $\text{MnO}_2/\text{PDA}$ ; (d) the linear fits of the  $\ln(R_{\text{ct}}^{-1})$  versus  $1000/T$

hydrogen bonds with protons at the interface with its functional groups such as amino and hydroxyl. This ensures the excellent rate capability of the  $\text{MnO}_2/\text{PDA}$  cathode.

The energy storage mechanisms of the cathodes are studied. Fig. 4a compares the XRD patterns of the  $\text{MnO}_2/\text{PDA}$  cathode at the charged and discharged states. The charged electrode presents diffractions from  $\text{MnO}_2$ , and extra diffractions from  $\text{Zn}_4\text{SO}_4(\text{OH})_6$  show up upon discharge. Besides, SEM images show nano-rods in the charged cathode and extra flakes are formed during discharge (Fig. 4b and c), which is the typical morphology for basic zinc salts.<sup>41</sup> This suggests proton involved

reactions during discharge, including proton intercalation and dissolution processes of  $\text{MnO}_2$  based on the following equation:  $\text{MnO}_2 + 4\text{H}^+ + 2\text{e}^- = \text{Mn}^{2+} + 2\text{H}_2\text{O}$ . The consumption of protons causes a local pH increase and  $\text{Zn}_4\text{SO}_4(\text{OH})_6$  precipitation. The recovery of  $\text{MnO}_2$  upon charge confirms a reversible cathode reaction. The nano-rod morphology is still retained after long-term cycling (Fig. S6†). Similar XRD and morphology evolutions are found for the bare  $\text{MnO}_2$  cathode (Fig. S7†).

The cycling stability of  $\text{MnO}_2$  materials is highly dependent on the active material dissolution/deposition phenomenon. To be more specific, the reduction of  $\text{MnO}_2$  during discharge would form  $\text{Mn}^{2+}$ , which easily dissolves in the electrolyte and causes active material loss. Nevertheless, if they can be reversibly deposited back to the cathode during charge, the active material can be effectively recycled. Meanwhile, this  $\text{MnO}_2/\text{Mn}^{2+}$  reaction is associated with two-electron transfers and adds capacity to the cathode. The above processes are evaluated for the two cathode materials by measuring the Mn concentration changes in the electrolytes at different states by using inductively coupled plasma (ICP, Fig. 4d). With the bare  $\text{MnO}_2$  cathode, the Mn concentrations in the electrolyte at the discharged and charged states are 148 mM and 48 mM, respectively. Notably, the Mn in the electrolyte at the charged state corresponds to the active material not able to deposit back,<sup>40</sup> and this irreversible loss of active material results in the fast capacity decay of  $\text{MnO}_2$  in zinc cells. With the  $\text{MnO}_2/\text{PDA}$  cathode, on the other hand, lower Mn concentrations are obtained at both states, *i.e.*, 108 mM and 6.5 mM, respectively. This suggests that PDA suppresses  $\text{Mn}^{2+}$  dissolution during discharge to some extent. Importantly, the low Mn concentration at the charged state demonstrates the reversible oxidation of dissolved  $\text{Mn}^{2+}$  and its re-deposition as  $\text{MnO}_2$  at the cathode. In order to further confirm the positive effect of PDA on  $\text{Mn}^{2+}$

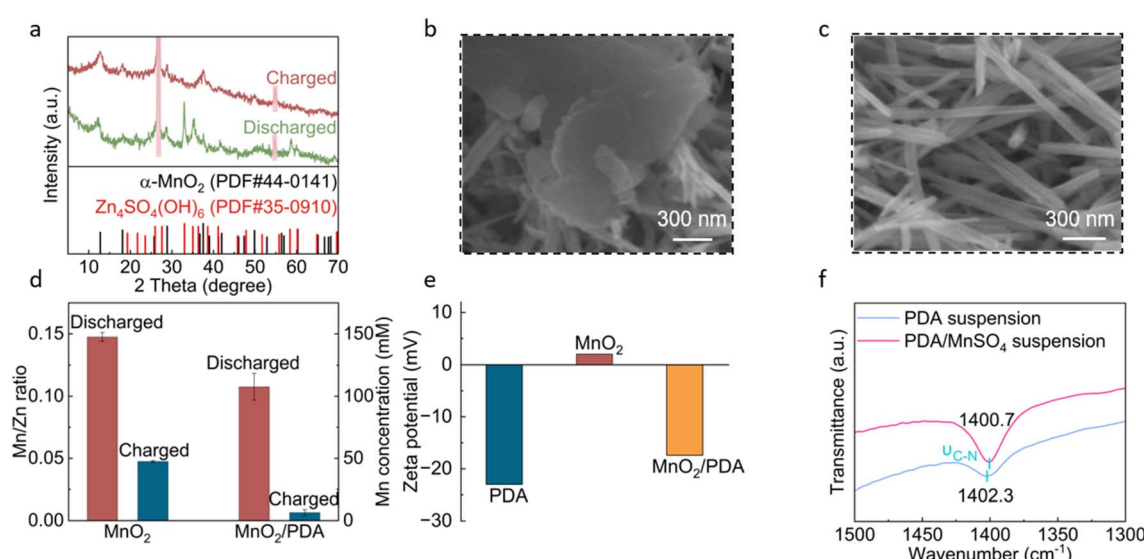


Fig. 4 (a) XRD patterns of the  $\text{MnO}_2/\text{PDA}$  cathode at different states (shaded peaks are from the carbon substrate). SEM images of the (b) discharged and (c) charged  $\text{MnO}_2/\text{PDA}$  cathode. (d) ICP results of Mn/Zn ratios and the calculated Mn concentrations in the 1 M  $\text{ZnSO}_4$  electrolyte at different states with the  $\text{MnO}_2$  and  $\text{MnO}_2/\text{PDA}$  cathodes. (e) The zeta potentials of PDA,  $\text{MnO}_2$  and  $\text{MnO}_2/\text{PDA}$ . (f) FT-IR of a PDA suspension in water and  $\text{MnSO}_4$  solution.

deposition, cells are assembled with cathodes of carbon cloth or carbon cloth coated with PDA (no  $\text{MnO}_2$  material) in the electrolyte  $1 \text{ M ZnSO}_4 + 0.1 \text{ M MnSO}_4$ . A constant voltage hold at  $2 \text{ V}$  is carried out to allow the oxidation of  $\text{Mn}^{2+}$  in the electrolyte and the deposition of  $\text{MnO}_2$  at the cathode. As shown in Fig. S8,<sup>†</sup> the current response of the carbon cloth electrode decays rapidly and drops below  $0.7 \text{ mA cm}^{-2}$  after only  $30 \text{ s}$ . In comparison, the current density of the PDA electrode decays much slower, and it takes  $1360 \text{ s}$  to drop below  $0.7 \text{ mA cm}^{-2}$ . The results verify the largely enhanced deposition reaction with the help of PDA. This recycles dissolved active material back to the cathode.

The functioning mechanism of PDA is studied. As discussed earlier in Fig. 1e and f, PDA and  $\text{MnO}_2$  exhibit strong coordination interactions. The FT-IR spectra of the  $\text{MnO}_2/\text{PDA}$  cathode at different states show the preservation of PDA vibration peaks (Fig. S9<sup>†</sup>), suggesting stable interactions during the electrochemical process. We further test the zeta potential of PDA,  $\text{MnO}_2$  and  $\text{MnO}_2/\text{PDA}$  (Fig. 4e). The  $\text{MnO}_2$  material itself shows a positive zeta potential of around  $2 \text{ mV}$ , whereas PDA exhibits a negative potential of  $-23.0 \text{ mV}$ . The  $\text{MnO}_2/\text{PDA}$  composite also exhibits a negative value of  $-17.4 \text{ mV}$ . This suggests a negatively charged surface with a PDA component, which provides electrostatic attraction for the dissolved  $\text{Mn}^{2+}$  cations. Fig. 4f and S10<sup>†</sup> compare the FT-IR spectra of a PDA suspension in water and  $\text{MnSO}_4$  solution. Although many vibrations from PDA are overlapped with those of water, the C–N vibration is identified and shows a redshift in  $\text{MnSO}_4$ . This is attributed to the coordination between PDA and  $\text{Mn}^{2+}$ , confirming their effective interactions. Therefore, although  $\text{Mn}^{2+}$  are still formed during the discharge process of the  $\text{MnO}_2/\text{PDA}$  cathode, these cations are linked with PDA species and gather around the cathode, resulting in a lower Mn concentration in the bulk electrolyte at the discharged state. Importantly, this strong interaction promotes the re-deposition of  $\text{Mn}^{2+}$  back to the cathode during the charge process. This retrieves the active material and ensures the stable long-term cycling of the  $\text{MnO}_2/\text{PDA}$  composite material.

## Conclusions

In summary, we present a PDA coating strategy to promote the cycling stability of the  $\text{MnO}_2$  cathode material in aqueous zinc batteries without relying on pre-added  $\text{Mn}^{2+}$  salts in electrolytes. FT-IR and Raman results confirm the coordination between nitrogen and oxygen sites on PDA with Mn components, and ICP reveals reduced Mn concentrations in the electrolyte at both discharged and charged states with the  $\text{MnO}_2/\text{PDA}$  composite cathode in comparison to bare  $\text{MnO}_2$ . This suggests that the strong interactions of PDA with Mn active material effectively confine the latter at the cathode and help the deposition of any dissolved species back to the cathode during the charge process. Therefore, the active material is well maintained for cathode reactions during the electrochemical process, which ensures a stable cycling performance. In aqueous zinc cells with the  $\text{ZnSO}_4$  electrolyte, the  $\text{MnO}_2/\text{PDA}$  composite cathode retains  $147 \text{ mA h g}^{-1}$  capacity after 2000

cycles at  $1 \text{ A g}^{-1}$ . This is superior to the bare  $\text{MnO}_2$  material, with only  $90 \text{ mA h g}^{-1}$  capacity left without the effects from PDA. Our work demonstrates an effective way to promote the cycling performance of manganese oxide electrode materials in aqueous zinc batteries. It could also be applied to other materials with dissolution problems.

## Data availability

Data are available from the authors on reasonable request.

## Author contributions

G. Z. and X. S. conceived and designed this work. G. Z. carried out the synthesis and electrochemical measurements. All authors participated in the analysis of the data, and discussed and revised the manuscript.

## Conflicts of interest

There are no conflicts to declare.

## Acknowledgements

This work was supported by the National Natural Science Foundation of China (52174276 and 51974070), the Fundamental Research Funds for the Central Universities (N2105001 and N232410019), and the 111 Project (B16009). Special thanks are due to the instrumental analysis from the Analytical and Testing Center, Northeastern University.

## References

- W. Shang, W. Yu, Y. Liu, R. Li, Y. Dai, C. Cheng, P. Tan and M. Ni, Rechargeable alkaline zinc batteries: Progress and challenges, *Energy Stor. Mater.*, 2020, **31**, 44–57.
- N. Dong, F. Zhang and H. Pan, Towards the practical application of Zn metal anodes for mild aqueous rechargeable Zn batteries, *Chem. Sci.*, 2022, **13**, 8243–8252.
- G. Ma, L. Miao, W. Yuan, K. Qiu, M. Liu, X. Nie, Y. Dong, N. Zhang and F. Cheng, Non-flammable, dilute, and hydrous organic electrolytes for reversible Zn batteries, *Chem. Sci.*, 2022, **13**, 11320–11329.
- J. Shin, J. Lee, Y. Park and J. W. Choi, Aqueous zinc ion batteries: focus on zinc metal anodes, *Chem. Sci.*, 2020, **11**, 2028–2044.
- Y. Chai, X. Xie, Z. He, G. Guo, P. Wang, Z. Xing, B. Lu, S. Liang, Y. Tang and J. Zhou, A smelting–rolling strategy for ZnIn bulk phase alloy anodes, *Chem. Sci.*, 2022, **13**, 11656–11665.
- J. S. Lee, S. Tai Kim, R. Cao, N. S. Choi, M. Liu, K. T. Lee and J. Cho, Metal–Air Batteries with High Energy Density: Li–Air versus Zn–Air, *Adv. Energy Mater.*, 2011, **1**, 34–50.
- N. Chang, Y. Yin, M. Yue, Z. Yuan, H. Zhang, Q. Lai and X. Li, A Cost-Effective Mixed Matrix Polyethylene Porous Membrane for Long-Cycle High Power Density Alkaline



Zinc-Based Flow Batteries, *Adv. Funct. Mater.*, 2019, **29**, 1901674.

8 D. Larcher and J. M. Tarascon, Towards greener and more sustainable batteries for electrical energy storage, *Nat. Chem.*, 2014, **7**, 19–29.

9 W. Li, A. Dolocan, P. Oh, H. Celio, S. Park, J. Cho and A. Manthiram, Dynamic behaviour of interphases and its implication on high-energy-density cathode materials in lithium-ion batteries, *Nat. Commun.*, 2017, **8**, 14589.

10 W. Sun, F. Wang, S. Hou, C. Yang, X. Fan, Z. Ma, T. Gao, F. Han, R. Hu, M. Zhu and C. Wang, Zn/MnO<sub>2</sub> Battery Chemistry With H<sup>+</sup> and Zn<sup>2+</sup> Coininsertion, *J. Am. Chem. Soc.*, 2017, **139**, 9775–9778.

11 M. Yan, P. He, Y. Chen, S. Wang, Q. Wei, K. Zhao, X. Xu, Q. An, Y. Shuang, Y. Shao, K. T. Mueller, L. Mai, J. Liu and J. Yang, Water-Lubricated Intercalation in V<sub>2</sub>O<sub>5</sub>·nH<sub>2</sub>O for High-Capacity and High-Rate Aqueous Rechargeable Zinc Batteries, *Adv. Mater.*, 2018, **30**, 1703725.

12 F. Wang, E. Hu, W. Sun, T. Gao, X. Ji, X. Fan, F. Han, X.-Q. Yang, K. Xu and C. Wang, A rechargeable aqueous Zn<sup>2+</sup>-battery with high power density and a long cycle-life, *Energy Environ. Sci.*, 2018, **11**, 3168–3175.

13 J. Shin, J. Lee, Y. Park and J. W. Choi, Aqueous zinc ion batteries: focus on zinc metal anodes, *Chem. Sci.*, 2020, **11**, 2028–2044.

14 T. Xue and H. J. Fan, From aqueous Zn-ion battery to Zn-MnO<sub>2</sub> flow battery: A brief story, *J. Energy Chem.*, 2021, **54**, 194–201.

15 Y. Zhang, Y. Liu, Z. Liu, X. Wu, Y. Wen, H. Chen, X. Ni, G. Liu, J. Huang and S. Peng, MnO<sub>2</sub> cathode materials with the improved stability *via* nitrogen doping for aqueous zinc-ion batteries, *J. Energy Chem.*, 2022, **64**, 23–32.

16 S. Yang, S. Zhao and S. Chen, Recent advances in electrospinning nanofiber materials for aqueous zinc ion batteries, *Chem. Sci.*, 2023, **14**, 13346–13366.

17 X. Jia, C. Liu, Z. G. Neale, J. Yang and G. Cao, Active Materials for Aqueous Zinc Ion Batteries: Synthesis, Crystal Structure, Morphology, and Electrochemistry, *Chem. Rev.*, 2020, **120**, 7795–7866.

18 Y. Liu, Z. Qin, X. Yang and X. Sun, A Long-Life Manganese Oxide Cathode Material for Aqueous Zinc Batteries with a Negatively Charged Porous Host to Promote the Back-Deposition of Dissolved Mn<sup>2+</sup>, *Adv. Funct. Mater.*, 2022, **32**, 2106994.

19 G. Fang, J. Zhou, A. Pan and S. Liang, Recent Advances in Aqueous Zinc-Ion Batteries, *ACS Energy Lett.*, 2018, **3**, 2480–2501.

20 P. He, G. Zhang, X. Liao, M. Yan, X. Xu, Q. An, J. Liu and L. Mai, Sodium Ion Stabilized Vanadium Oxide Nanowire Cathode for High-Performance Zinc-Ion Batteries, *Adv. Energy Mater.*, 2018, **8**, 1702463.

21 P. He, Q. Chen, M. Yan, X. Xu, L. Zhou, L. Mai and C.-W. Nan, Building better zinc-ion batteries: A materials perspective, *EnergyChem*, 2019, **1**, 100022.

22 N. Zhang, X. Chen, M. Yu, Z. Niu, F. Cheng and J. Chen, Materials chemistry for rechargeable zinc-ion batteries, *Chem. Soc. Rev.*, 2020, **49**, 4203–4219.

23 V. Mathew, B. Sambandam, S. Kim, S. Kim, S. Park, S. Lee, M. H. Alfaruqi, V. Soundharajan, S. Islam, D. Y. Putro, J.-Y. Hwang, Y.-K. Sun and J. Kim, Manganese and Vanadium Oxide Cathodes for Aqueous Rechargeable Zinc-Ion Batteries: A Focused View on Performance, Mechanism, and Developments, *ACS Energy Lett.*, 2020, **5**, 2376–2400.

24 J. Li, Y. Chen, J. Guo, F. Wang, H. Liu and Y. Li, Graphdiyne Oxide-Based High-Performance Rechargeable Aqueous Zn-MnO<sub>2</sub> Battery, *Adv. Funct. Mater.*, 2020, **30**, 2004115.

25 H. Pan, Y. Shao, P. Yan, Y. Cheng, K. S. Han, Z. Nie, C. Wang, J. Yang, X. Li, P. Bhattacharya, K. T. Mueller and J. Liu, Reversible aqueous zinc/manganese oxide energy storage from conversion reactions, *Nat. Energy*, 2016, **1**, 16039.

26 J. Huang, Z. Wang, M. Hou, X. Dong, Y. Liu, Y. Wang and Y. Xia, Polyaniline-intercalated manganese dioxide nanolayers as a high-performance cathode material for an aqueous zinc-ion battery, *Nat. Commun.*, 2018, **9**, 2906.

27 M. Zhang, W. Wu, J. Luo, H. Zhang, J. Liu, X. Liu, Y. Yang and X. Lu, A high-energy-density aqueous zinc–manganese battery with a La–Ca co-doped ε-MnO<sub>2</sub> cathode, *J. Mater. Chem. A*, 2020, **8**, 11642–11648.

28 J. Yang, G. Yao, Z. Li, Y. Zhang, L. Wei, H. Niu, Q. Chen and F. Zheng, Highly Flexible K-Intercalated MnO<sub>2</sub>/Carbon Membrane for High-Performance Aqueous Zinc-Ion Battery Cathode, *Small*, 2023, **19**, 2205544.

29 X. Shen, X. Wang, Y. Zhou, Y. Shi, L. Zhao, H. Jin, J. Di and Q. Li, Highly Reversible Aqueous Zn-MnO<sub>2</sub> Battery by Supplementing Mn<sup>2+</sup>-Mediated MnO<sub>2</sub> Deposition and Dissolution, *Adv. Funct. Mater.*, 2021, **31**, 2101579.

30 Z. Li, Y. Li, X. Ren, Y. Zhao, Z. Ren, Z. Yao, W. Zhang, H. Xu, Z. Wang, N. Zhang, Y. Gu, X. Li, D. Zhu and J. Zou, Elucidating the Reaction Mechanism of Mn<sup>2+</sup> Electrolyte Additives in Aqueous Zinc Batteries, *Small*, 2023, **19**, 2301770.

31 D. Chao, W. Zhou, C. Ye, Q. Zhang, Y. Chen, L. Gu, K. Davey and S. Z. Qiao, An Electrolytic Zn-MnO<sub>2</sub> Battery for High-Voltage and Scalable Energy Storage, *Angew. Chem., Int. Ed.*, 2019, **58**, 7823–7828.

32 T. Xiong, Z. G. Yu, H. Wu, Y. Du, Q. Xie, J. Chen, Y. W. Zhang, S. J. Pennycook, W. S. V. Lee and J. Xue, Defect Engineering of Oxygen-Deficient Manganese Oxide to Achieve High-Performing Aqueous Zinc Ion Battery, *Adv. Energy Mater.*, 2019, **9**, 1803815.

33 Y. Liu, K. Wang, X. Yang, J. Liu, X.-X. Liu and X. Sun, Enhancing Two-Electron Reaction Contribution in MnO<sub>2</sub> Cathode Material by Structural Engineering for Stable Cycling in Aqueous Zn Batteries, *ACS Nano*, 2023, **17**, 14792–14799.

34 Z. He, S. Liu, Y. Zhong, D. Chen, H. Ding, J. Wang, G. Du, G. Yang and Q. Hao, Preparation of BiPO<sub>4</sub>/graphene photoelectrode and its photoelectrocatalytic performance, *Chin. J. Catal.*, 2020, **41**, 302–311.

35 J. Yang, D. Chen, Y. Zhu, Y. Zhang and Y. Zhu, 3D-3D porous Bi<sub>2</sub>WO<sub>6</sub>/graphene hydrogel composite with excellent synergistic effect of adsorption-enrichment and



photocatalytic degradation, *Appl. Catal., B*, 2017, **205**, 228–237.

36 T. Wang, P. Wang, L. Pan, Z. He, L. Dai, L. Wang, S. Liu, S. C. Jun, B. Lu, S. Liang and J. Zhou, Stabilizing Zinc Metal Anode with Polydopamine Regulation through Dual Effects of Fast Desolvation and Ion Confinement, *Adv. Energy Mater.*, 2023, **13**, 2203523.

37 F. Wu, X. Gao, X. Xu, Y. Jiang, X. Gao, R. Yin, W. Shi, W. Liu, G. Lu and X. Cao,  $\text{MnO}_2$  Nanosheet-Assembled Hollow Polyhedron Grown on Carbon Cloth for Flexible Aqueous Zinc-Ion Batteries, *ChemSusChem*, 2020, **13**, 1537–1545.

38 J.-W. Xu, Q.-L. Gao, Y.-M. Xia, X.-S. Lin, W.-L. Liu, M.-M. Ren, F.-G. Kong, S.-J. Wang and C. Lin, High-performance reversible aqueous zinc-ion battery based on iron-doped alpha-manganese dioxide coated by polypyrrole, *J. Colloid Interface Sci.*, 2021, **598**, 419–429.

39 X. Lu, D. Zheng, T. Zhai, Z. Liu, Y. Huang, S. Xie and Y. Tong, Facile synthesis of large-area manganese oxide nanorod arrays as a high-performance electrochemical supercapacitor, *Energy Environ. Sci.*, 2011, **4**, 2915–2921.

40 Y. Liu, Z. Qin, X. Yang, J. Liu, X.-X. Liu and X. Sun, Voltage induced lattice contraction enabling superior cycling stability of  $\text{MnO}_2$  cathode in aqueous zinc batteries, *Energy Stor. Mater.*, 2023, **56**, 524–531.

41 Y. Liu, X. Zhou, R. Liu, X. Li, Y. Bai, H. Xiao, Y. Wang and G. Yuan, Tailoring Three-Dimensional Composite Architecture for Advanced Zinc-Ion Batteries, *ACS Appl. Mater. Interfaces*, 2019, **11**, 19191–19199.

